Capítulo 9

Transformações de fase pós-solidificação

Serão abordadas duas transformações no estado sólido:

- A primeira envolve a transformação da ferrita em austenita nos aços inox. austeníticos .
- A segunda a transformação da asutenita em ferrita nos aços baixo carbono e/ou baixa liga.

Transformação Inox. Austeníticos

- Solda de Inox. Austenítico (γ) em geral apresenta estrutura mista γ + ferrita δ.
- Quando a ferrita $\delta > 10\%$ ocorre redução da ductilidade.
- Quando a ferrita $\delta < 5\ \%$ risco de ocorrer trincas de solidificação.

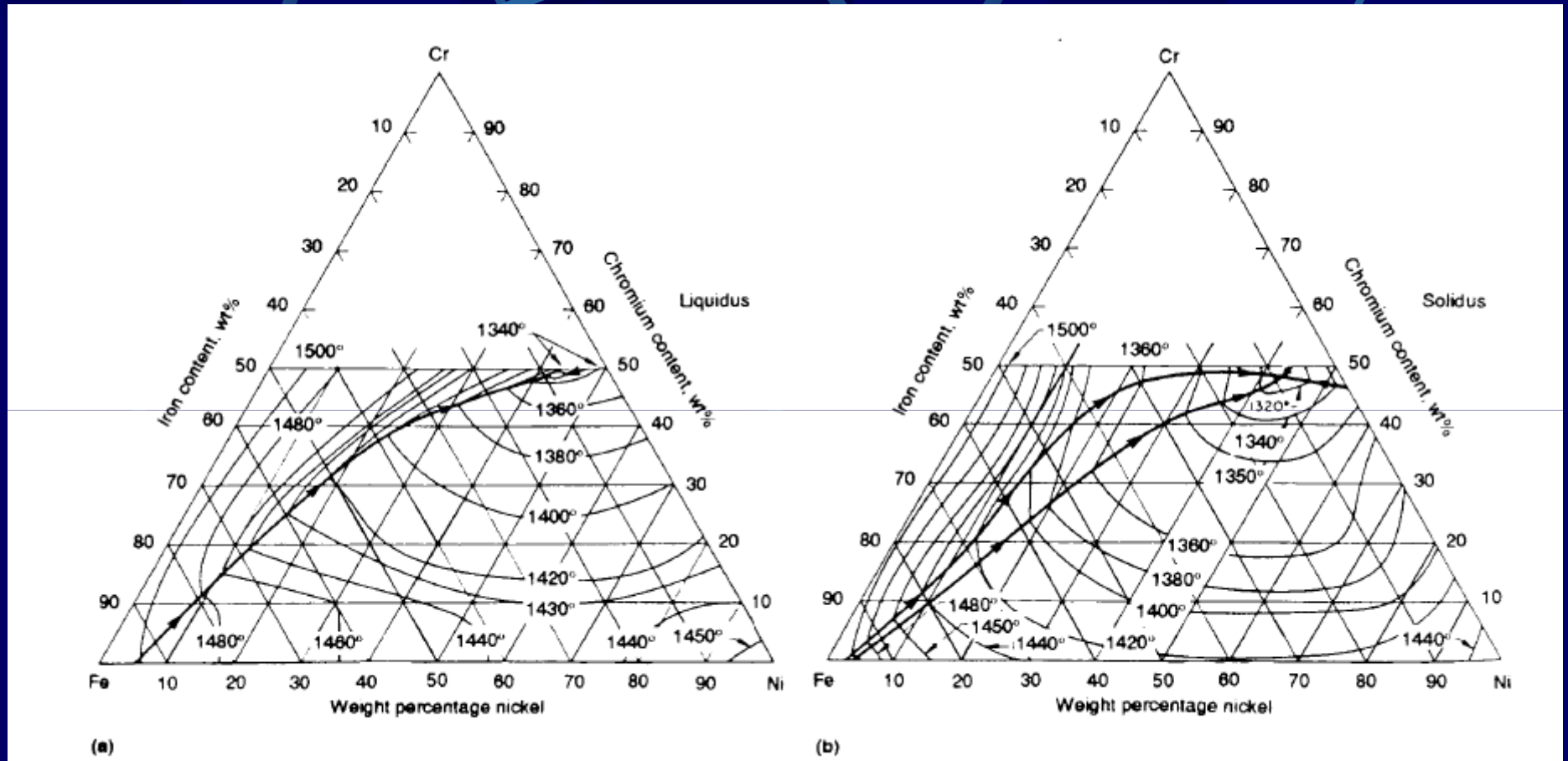

Figure 9.1 The Fe–Cr–Ni ternary system: (*a*) liquidus surface; (*b*) solidus surface. Reprinted from *Metals Handbook* (8).

Diagrama pseudo-binário 70%Fe Cr Ni

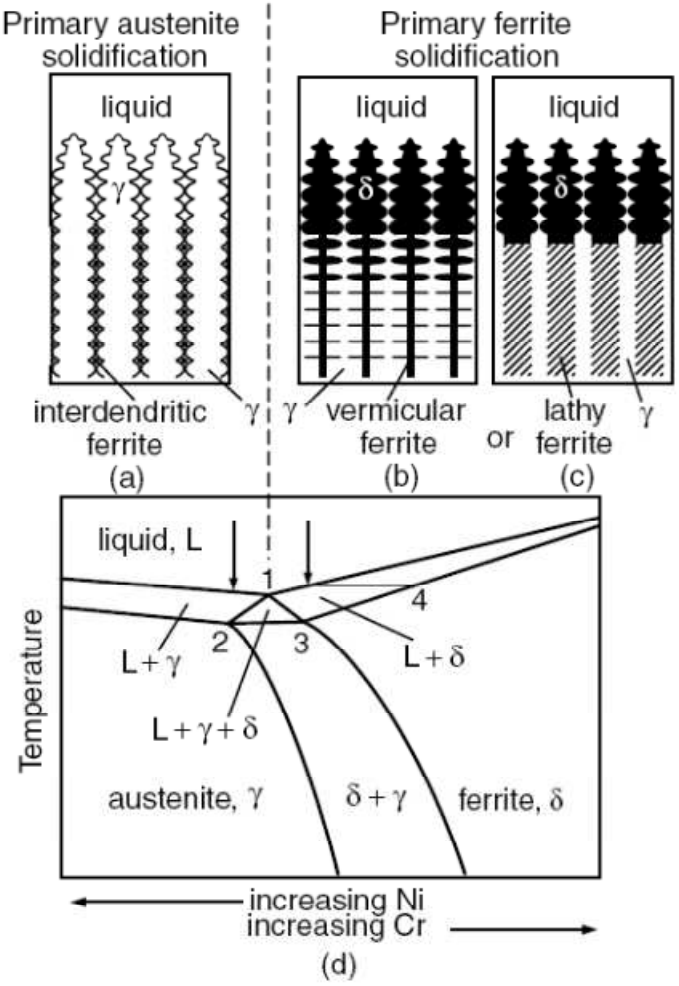

Figure 9.2 Schematics showing solidification and postsolidification transformation in Fe–Cr–Ni welds: (*a*) interdendritic ferrite; (*b*) vermicular ferrite; (*c*) lathy ferrite; (*d*) vertical section of ternary-phase diagram at approximately 70% Fe.

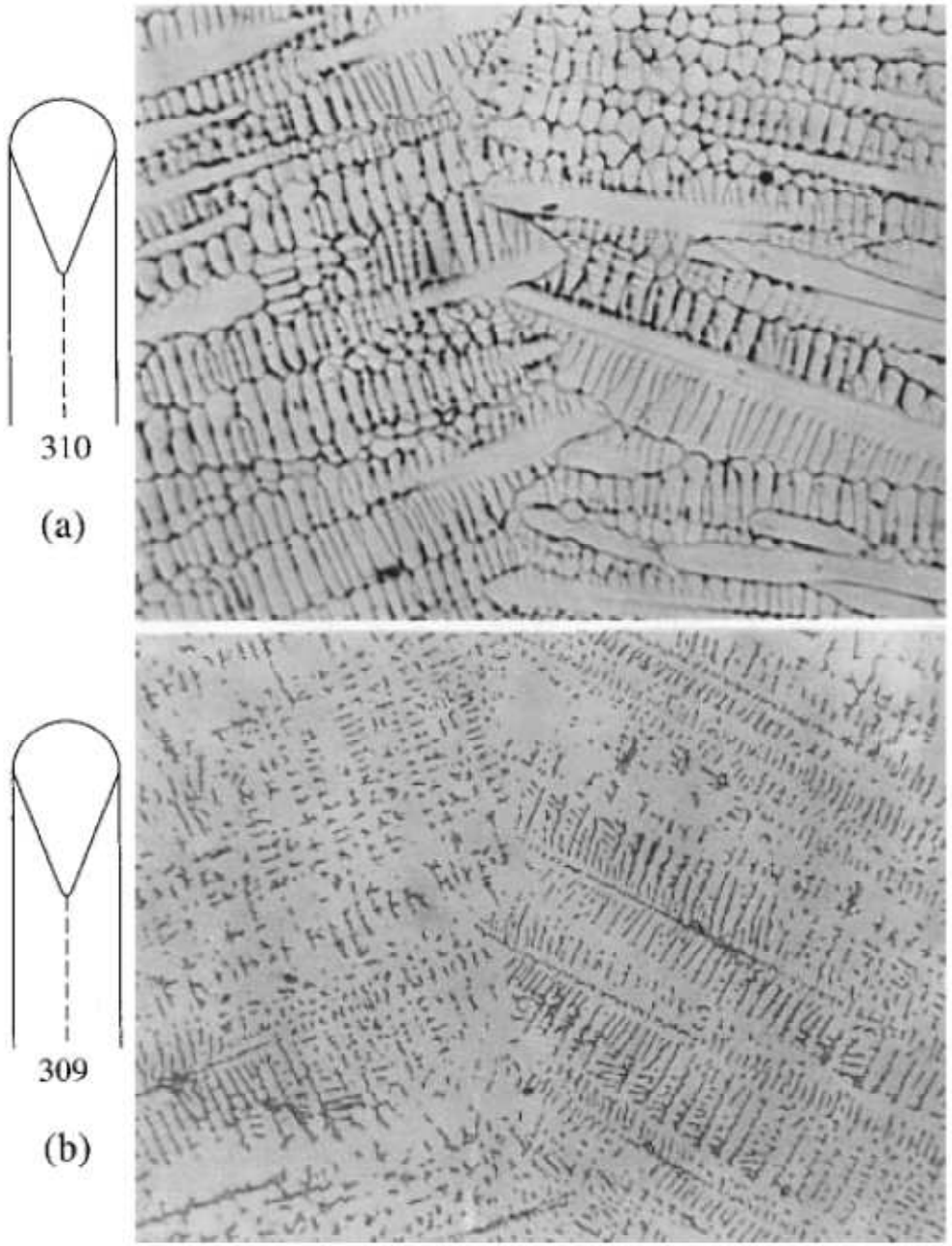

Figure 9.3 Solidification structure at the weld centerline: (*a*) 310 stainless steel; (*b*) 309 stainless steel. Magnification 190×. Reprinted from Kou and Le (9).

310 309

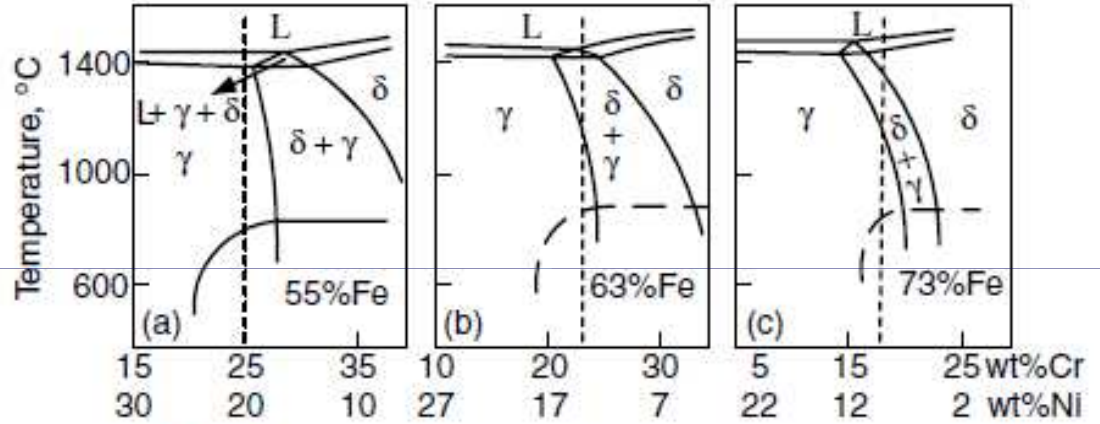

Figure 9.4 The Fe–Cr–Ni pseudo-binary phase diagrams: (*a*) at 55 wt % Fe; (*b*) at 63 wt % Fe; (*c*) at 73 wt % Fe. Reprinted from Kou and Le (9).

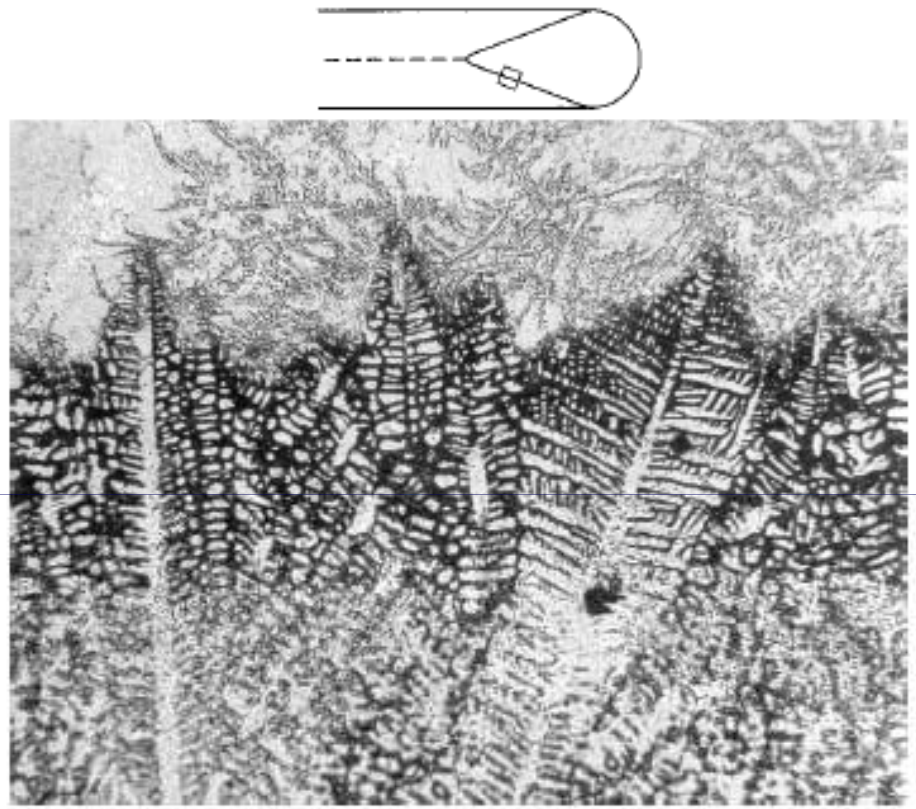

Figure 9.5 Liquid-tin quenched solidification structure near the pool of an autogenous gas–tungsten arc weld of 309 stainless steel. Magnification 70×. Mixed-chloride etchant. Reprinted from Kou and Le (9).

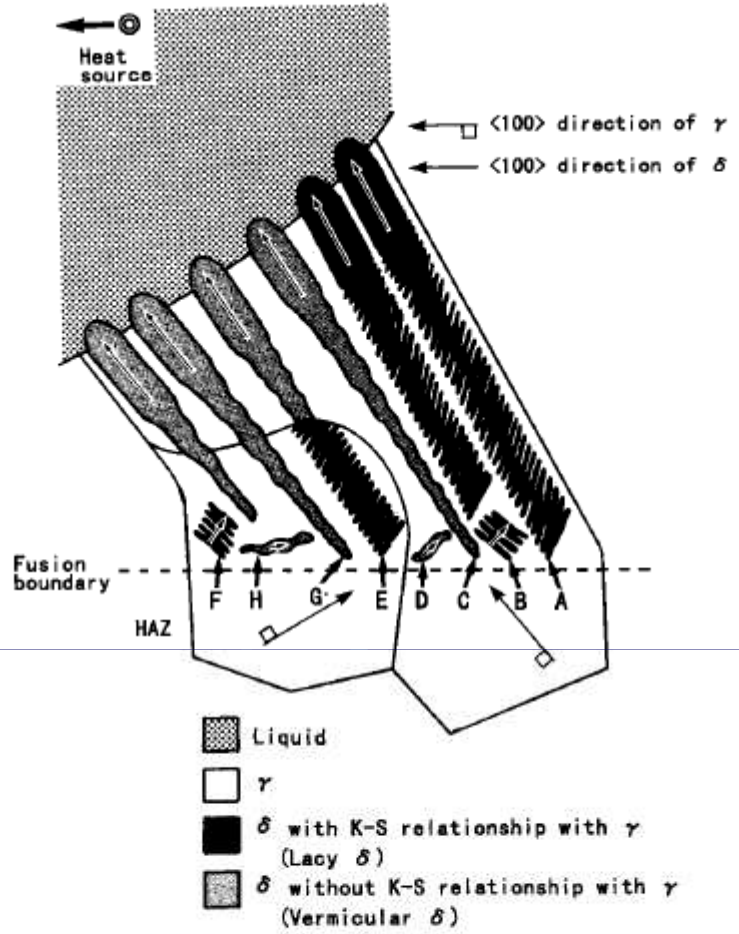

Figure 9.6 Mechanism for the formation of vermicular and lathy ferrite. Reprinted from Inoue et al. (11).

Kurdjumov-Sachs $\longrightarrow$ $(\bar{1}10)_\delta // (\bar{1}11)_\gamma$ and $[\bar{1}\bar{1}1]_\delta // [\bar{1}\bar{1}0]_\gamma$

Diagrama de Schaeffler

Identifica a microestrutura dos aços inoxidáveis em função dos elementos austenitizantes (Ni, Mn, C) X ferritizantes (Cr, Mo, Si, Cb).

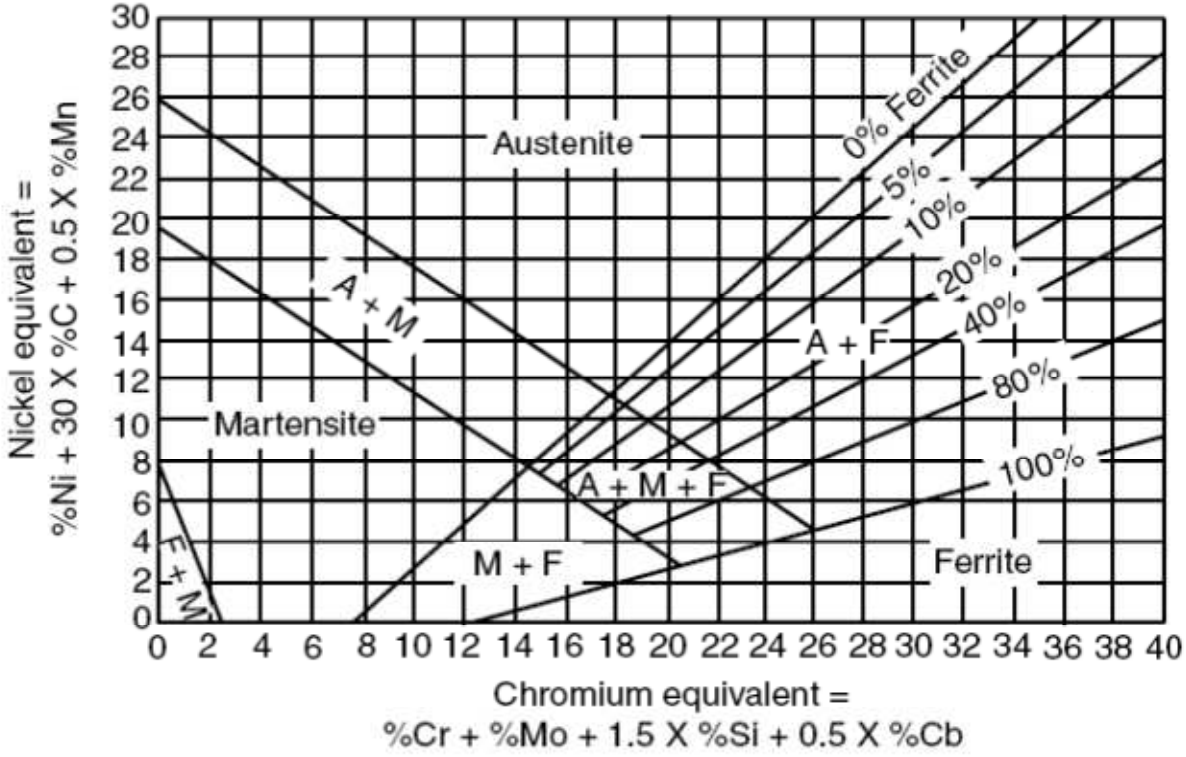

Figure 9.8 Schaeffler diagram for predicting weld ferrite content and solidification mode. From Schaeffler (12).

Diagrama de DeLong

- Diagrama de Schaeffler “refinado”,
- Inclui N como elemento austenitizante.
- Ferrita identificada como *Ferrite Number*

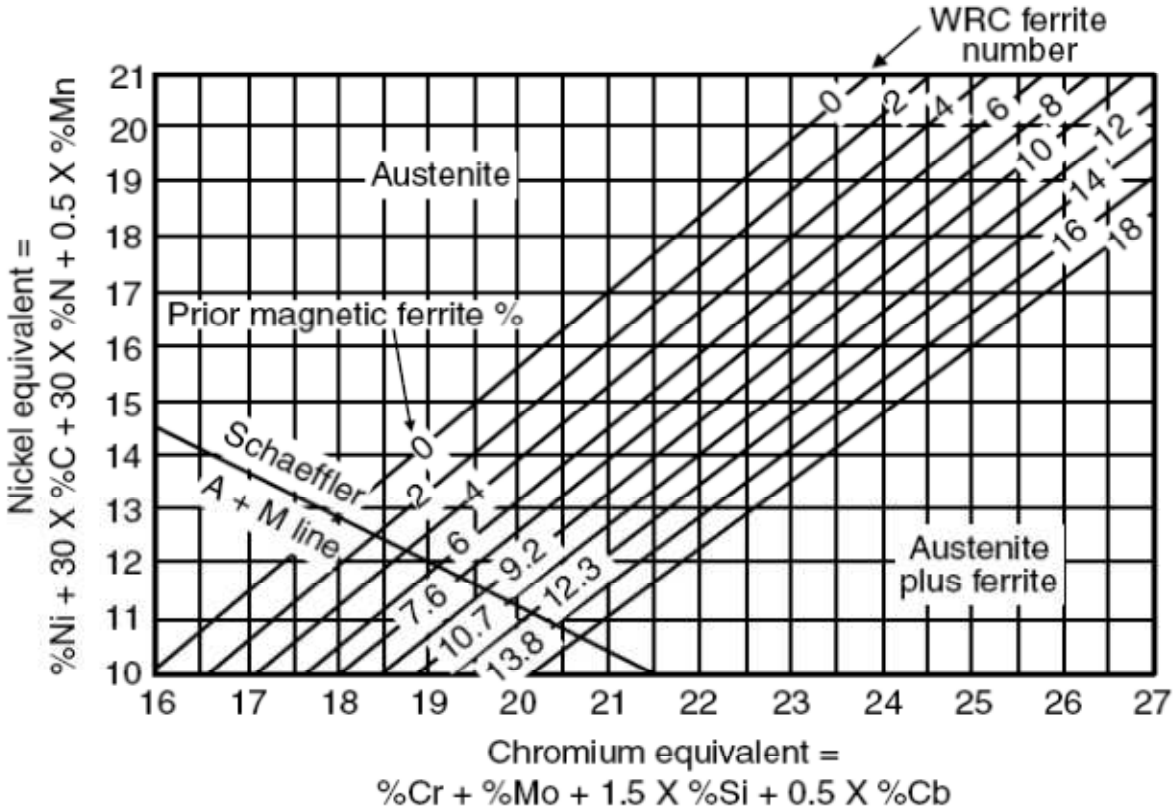

Figure 9.9 DeLong diagram for predicting weld ferrite content and solidification mode. Reprinted from DeLong (13). Courtesy of American Welding Society.

Efeito do Nitrogênio

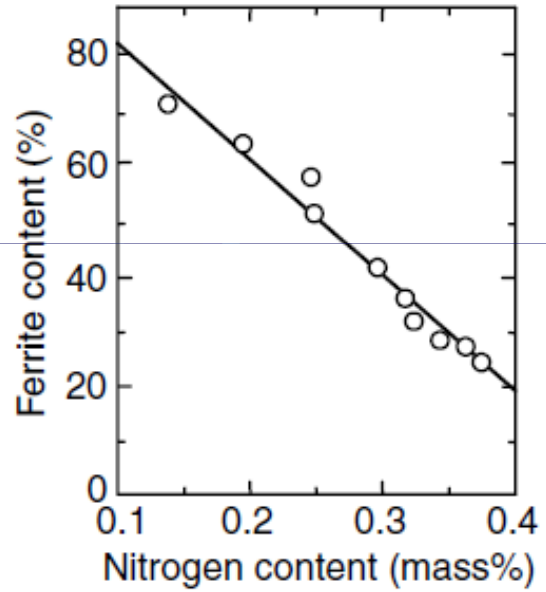

Figure 9.10 Effect of nitrogen on ferrite content in gas–tungsten arc welds of duplex stainless steel. Reprinted from Sato et al. (14).

Efeito do Nitrogênio

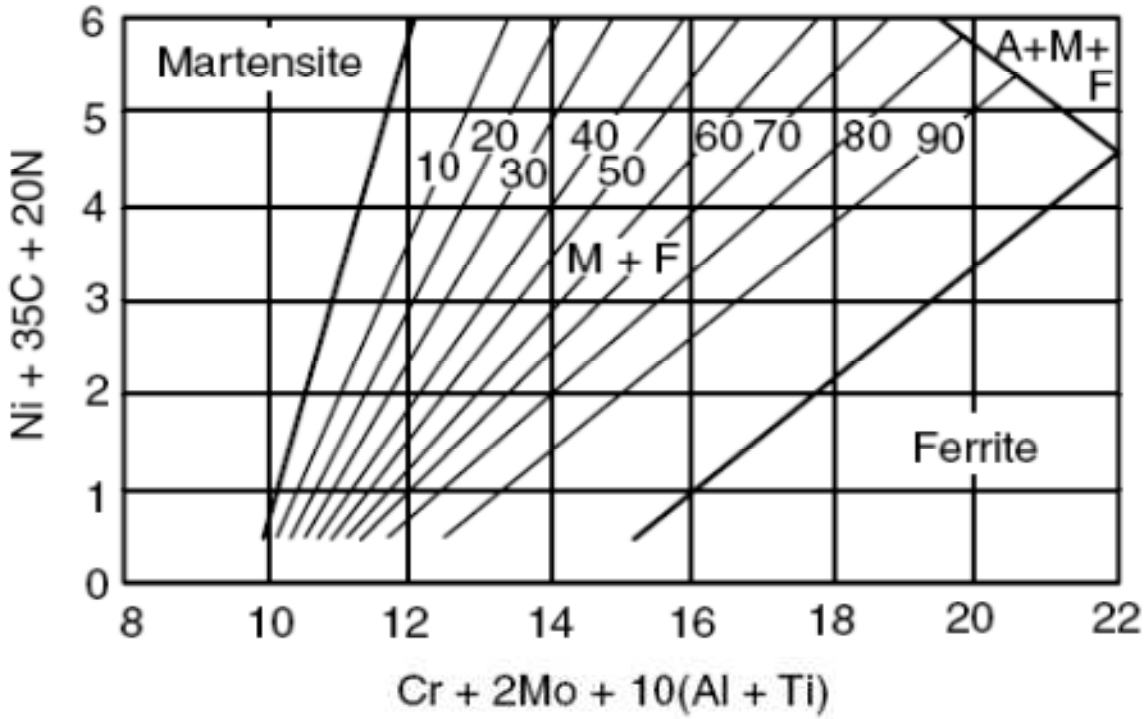

Figure 9.13 Ferritic–martensitic stainless steel constitution diagram containing a boundary for austenite formation and with iso-ferrite lines in volume percent of ferrite. Reprinted from Balmforth and Lippold (23).

WRC-1992 *World Research Council*

- Diagrama de Schaeffler “refinado” para determinação da ferrita.
- Inclui N e Cu como elementos austenitizantes.
- Ferrita identificada como *Ferrite Number*

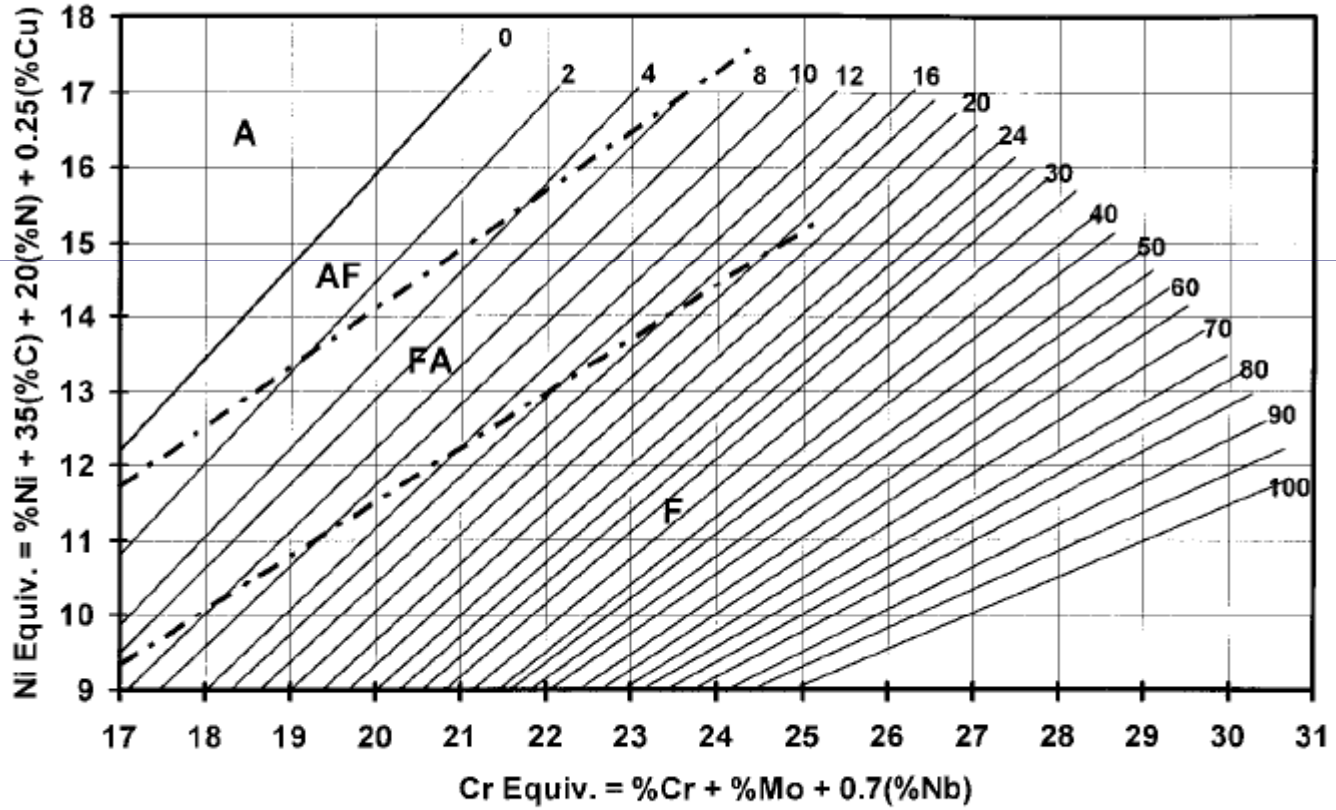

Figure 9.11 WRC-1992 diagram for predicting weld ferrite content and solidification mode. Reprinted from Kotecki and Siewert (16). Courtesy of American Welding Society.

WRC- 1992 *World Research Council*

- Diagrama de Schaeffler “refinado” para determinação da ferrita.
- Inclui N e Cu como elementos austenitizantes.
- Ferrita identificada como *Ferrite Number*

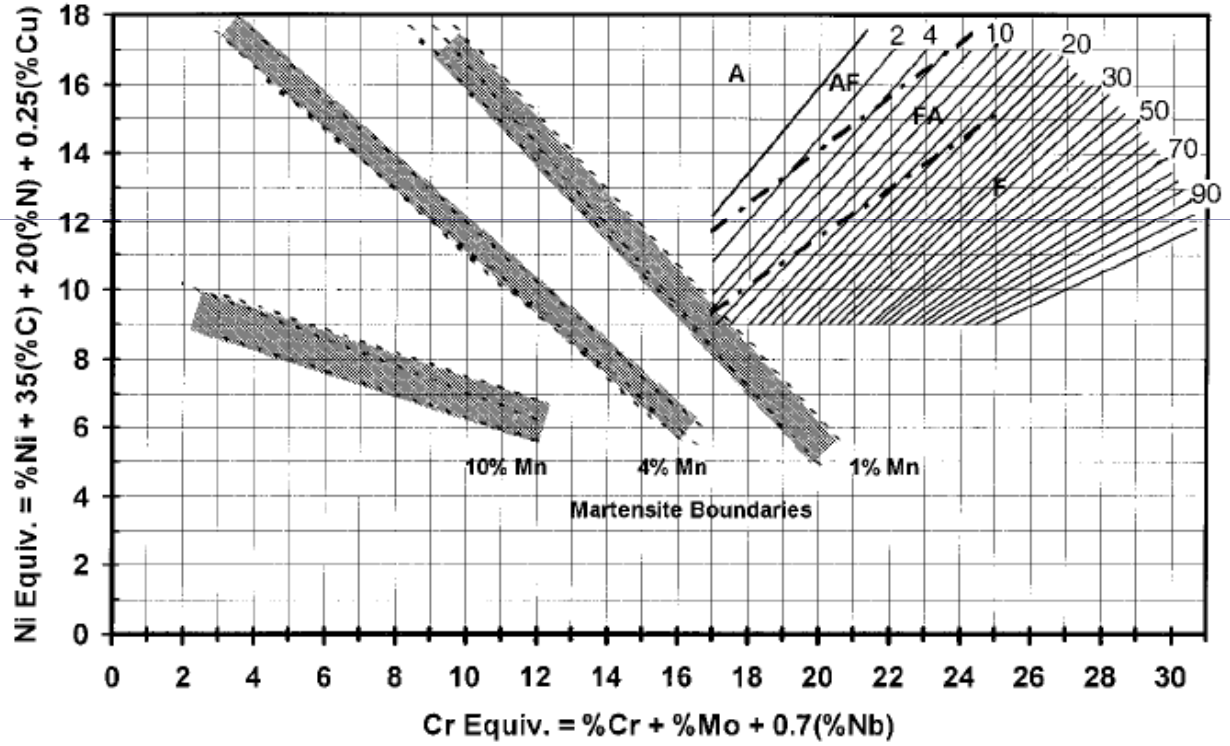

Figure 9.12 WRC-1992 diagram with martensite boundaries for 1, 4, and 10% Mn. Reprinted from Kotecki (20). Courtesy of American Welding Society.

Efeito da taxa de resfriamento

- Para a relação Cr/Ni baixa, a % de ferrita δ diminui com o aumento da taxa de resfriamento.
- Para a relação Cr/Ni alta, a % de ferrita δ aumenta com o aumento da taxa de resfriamento.

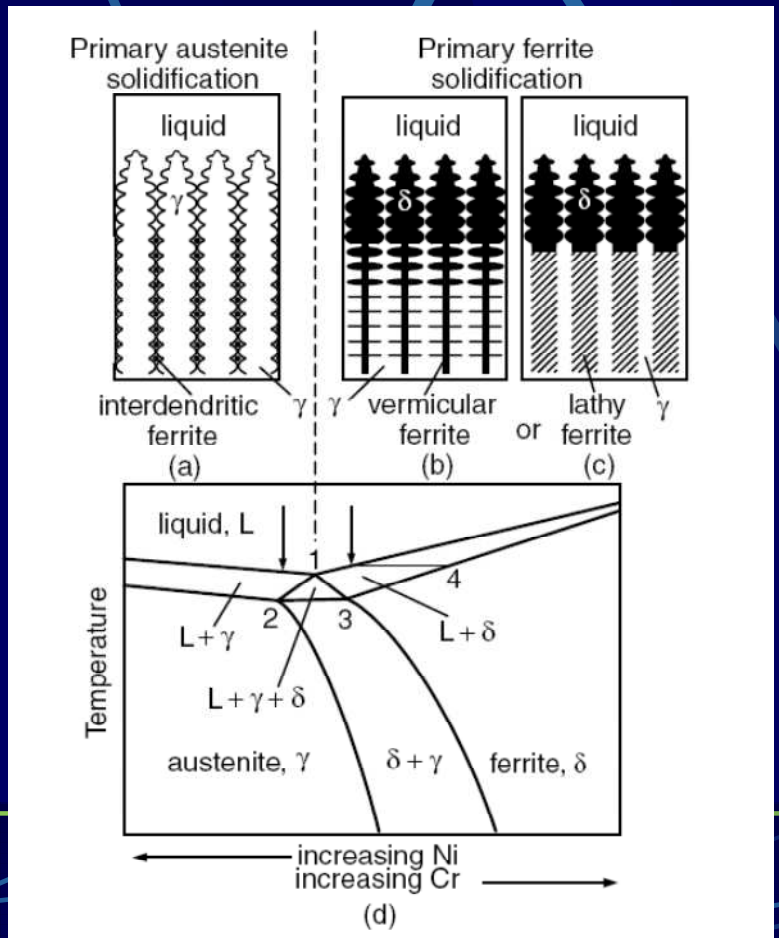

Efeito da taxa de resfriamento

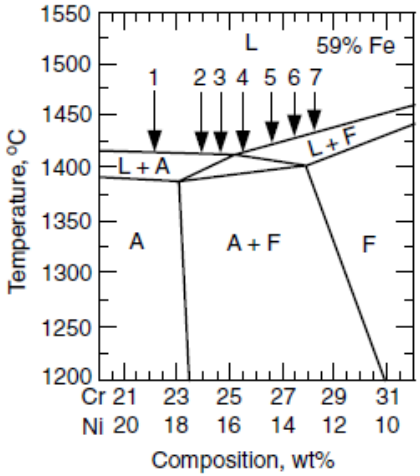

Figure 9.15 Vertical section of Fe–Ni–Cr phase diagram at 59% Fe showing seven alloys with Cr–Ni ratio ranging from 1.15 to 2.18. Modified from Elmer et al. (33).

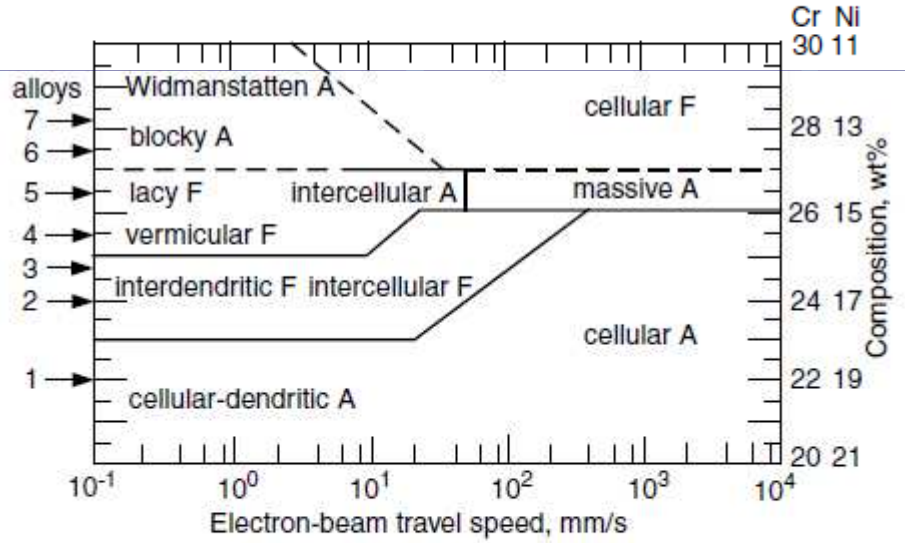

Figure 9.16 Electron beam travel speed (cooling rate) versus composition map of microstructural morphologies of the seven alloys in Figure 9.15 (A and F denote austenite and ferrite, respectively). The solid lines indicate the regions of the four primary solidification modes, while the dashed lines represent the different morphologies resulting from postsolidification transformation from ferrite to austenite. Modified from Elmer et al. (33).

Efeito da taxa de resfriamento

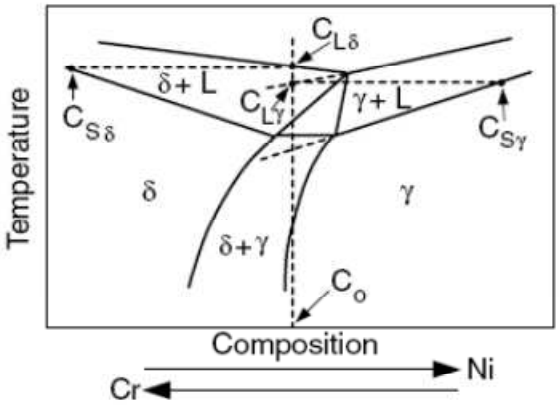

Figure 9.18 Vertical section of Fe–Cr–Ni phase diagram showing change in solidification from ferrite to austenite due to dendrite tip undercooling. Reprinted from Brooks and Thompson (37).

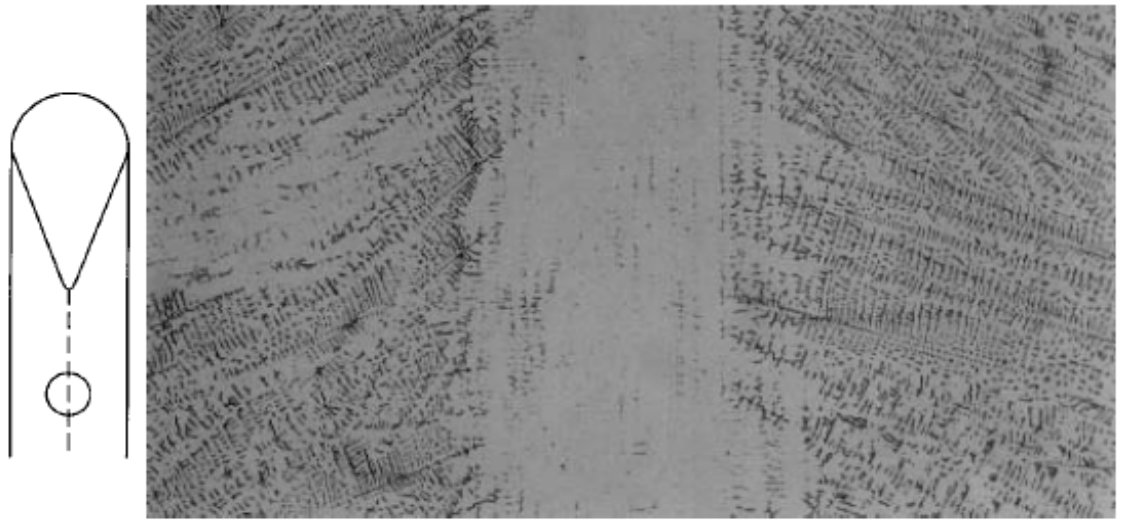

Figure 9.19 Weld centerline austenite in an autogenous gas–tungsten arc weld of 309 stainless steel solidified as primary ferrite. From Kou and Le (9).

Dissolução da ferrita δ devido ao reaquecimento - multipasses

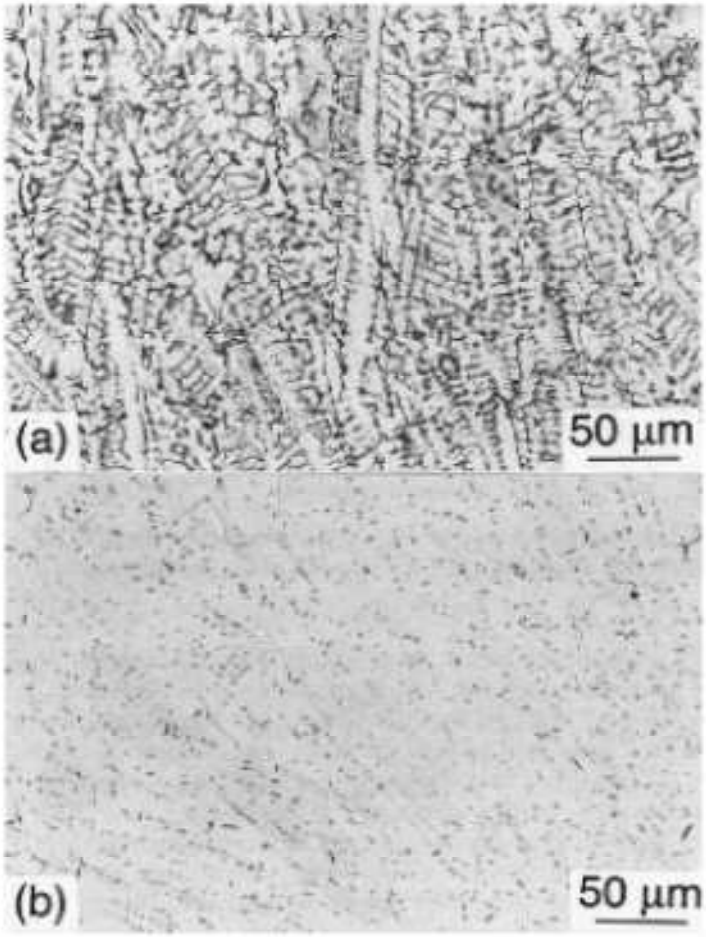

Figure 9.20 Effect of thermal cycles on ferrite content in 316 stainless steel weld: (*a*) as welded; (*b*) subjected to thermal cycle of 1250°C peak temperature three times after welding. Reprinted from Chen and Chou (40).

Transformação Aços baixo C e/ou baixa liga.

Diagrama TTT contínuo (simplificado)
Fase desejável Ferrita acicular –melhor tenacidade

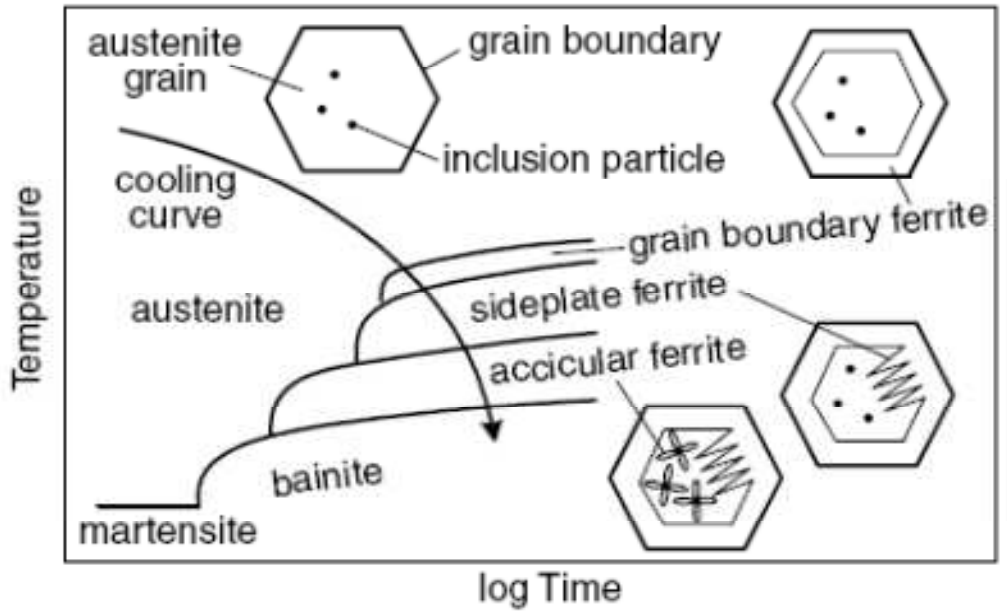

Figure 9.21 Continuous-cooling transformation diagram for weld metal of low-carbon steel.

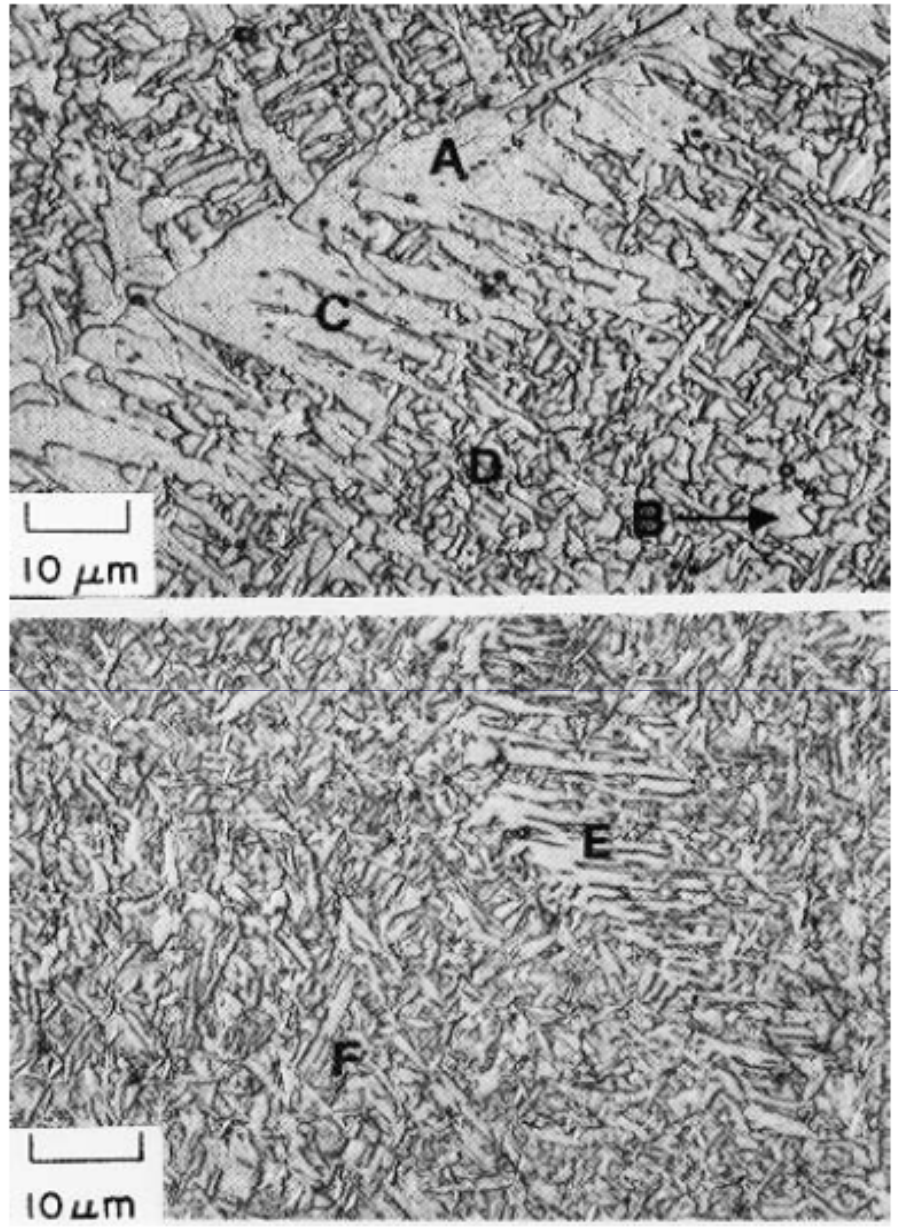

Figure 9.22 Micrographs showing typical weld metal microstructures in low-carbon steels: A, grain boundary ferrite; B, polygonal ferrite; C, Widmanstatten ferrite; D, acicular ferrite; E, upper bainite; F, lower bainite. Reprinted from Grong and Matlock (46).

Ferrita acicular.

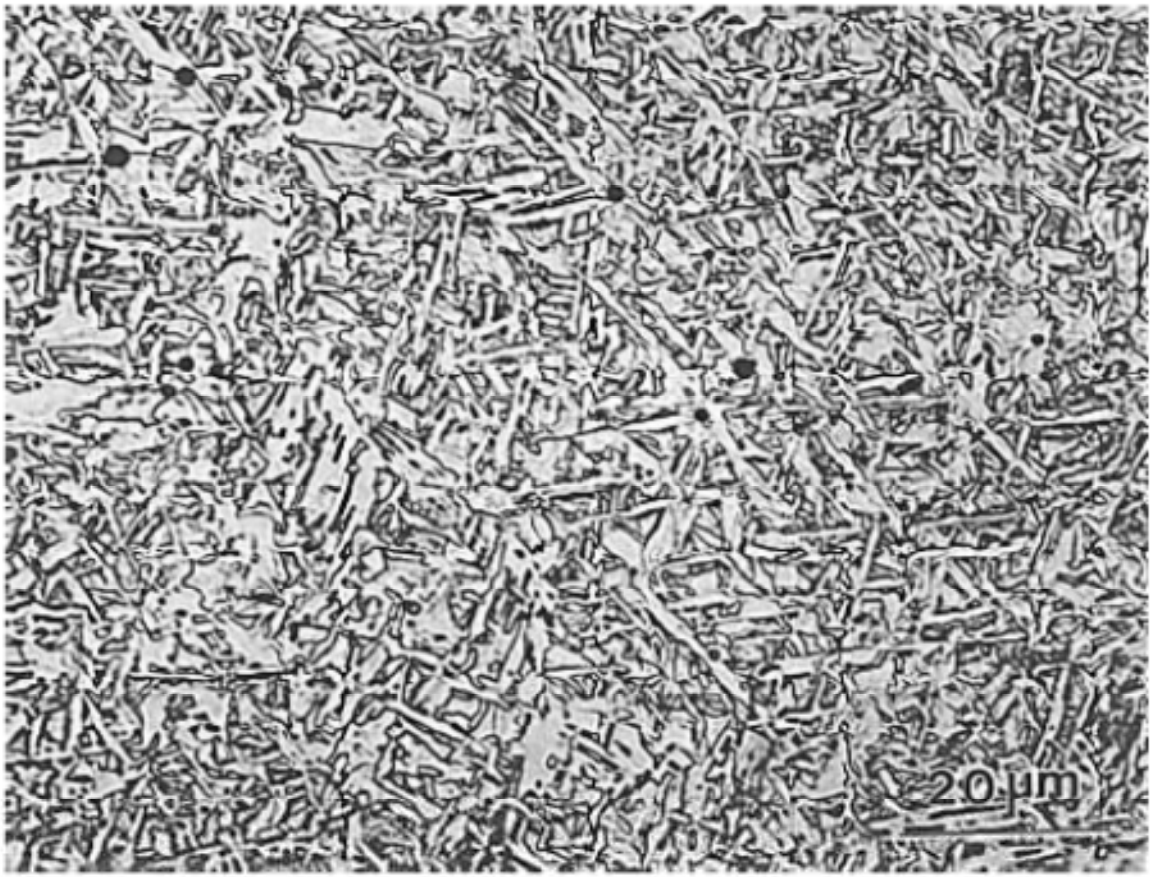

Figure 9.23 Predominately acicular ferrite microstructure of a low-carbon, low-alloy steel weld. Reprinted from Babu et al. (47).

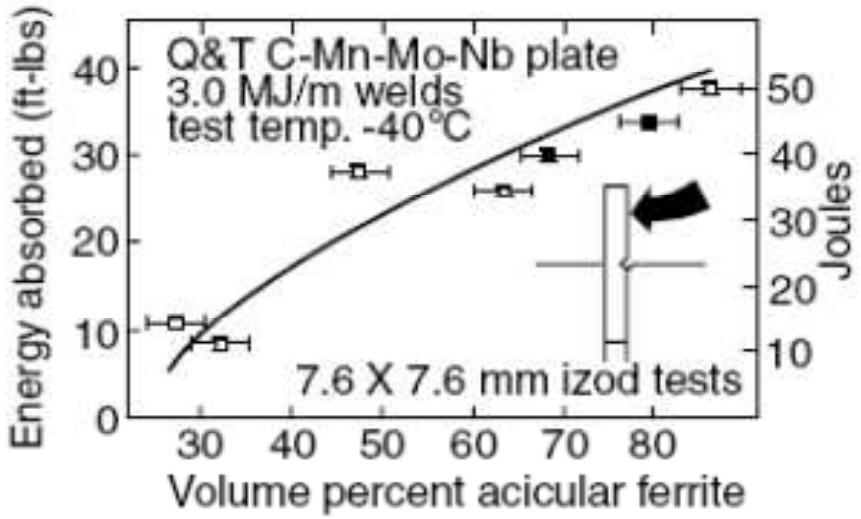

Figure 9.29 Subsize Charpy V-notch toughness values as a function of volume fraction of acicular ferrite in submerged arc welds. Reprinted from Fleck et al. (49). Courtesy of American Welding Society.

Fatores que afetam a microestrutura.

a) Tempo de resfriamento Δt 800-500 °C (Δt_{8-5})
Considere a primeira TTTc a esquerda. A medida que a taxa de resfriamento diminui, curvas 1, 2 e 3, a microestrutura muda de bainita, ferrita acicular ou ferrita de Widmanstätten.

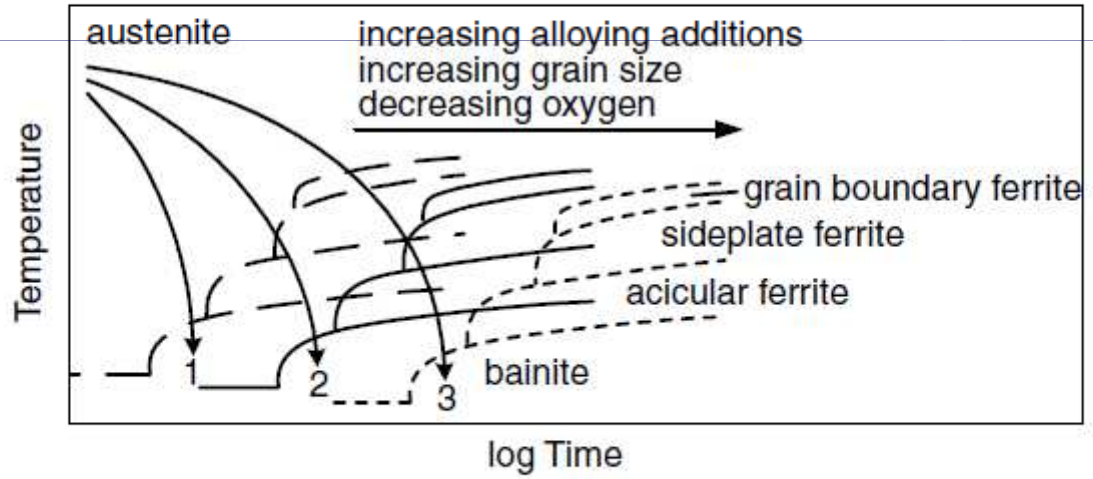

Figure 9.26 Effect of alloying elements, grain size, and oxygen on CCT diagrams for weld metal of low-carbon steel.

Fatores que afetam a microestrutura.

b) Elementos de liga

Adição de elementos de liga desloca a curva TTTc para a direita. Considerando a curva 3, a microestrutura muda de Ferrita de Widmanstätten para ferrita acicular e bainita dependendo do deslocamento, ou seja, da quantidade de elementos de liga no aço.

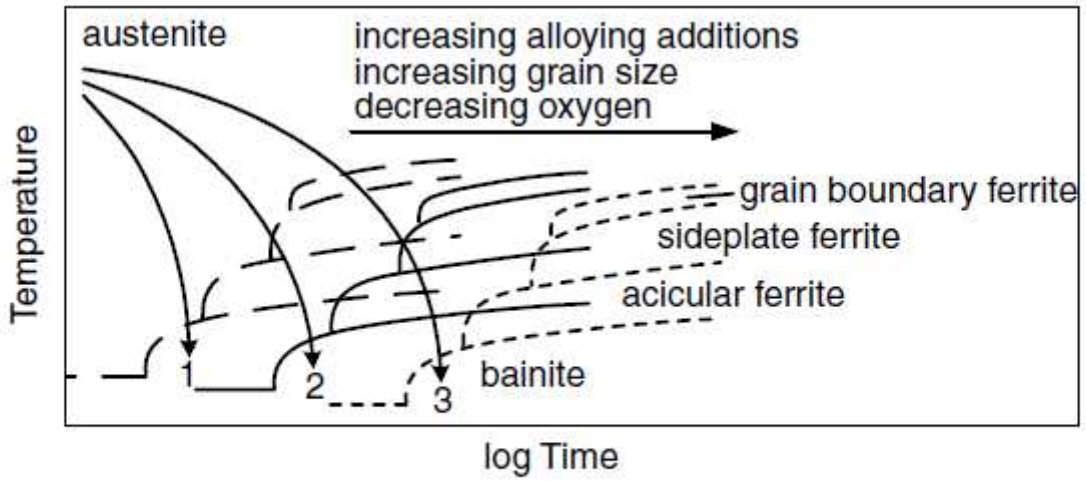

Figure 9.26 Effect of alloying elements, grain size, and oxygen on CCT diagrams for weld metal of low-carbon steel.

Fatores que afetam a microestrutura.

c) Tamanho de grão

Similar à adição de elementos de liga.Quanto maior o tamanho de grão mais deslocada a curva TTTc para a direita.
Considerando a curva 3, a microestrutura muda de Ferrita de Widmanstätten para ferrita acicular e bainita.

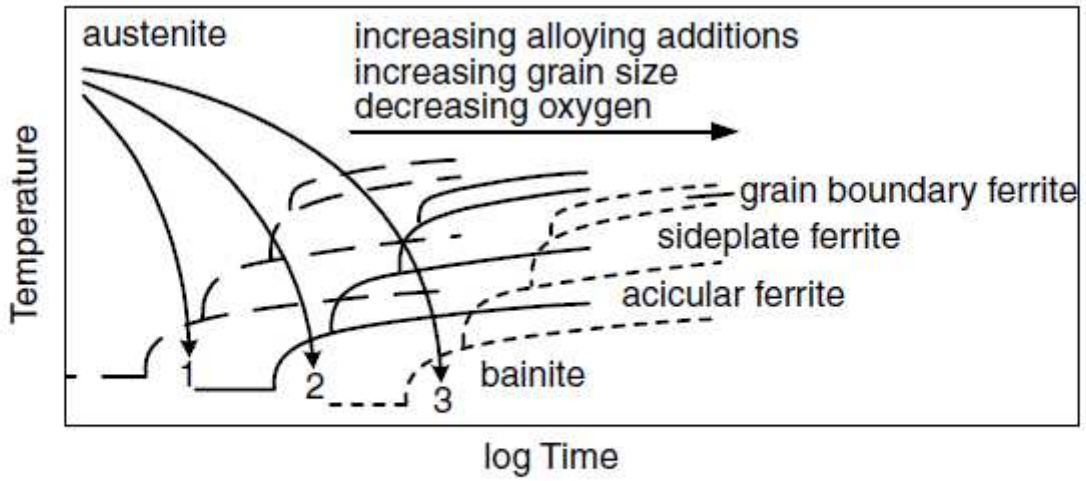

Figure 9.26 Effect of alloying elements, grain size, and oxygen on CCT diagrams for weld metal of low-carbon steel.

Fatores que afetam a microestrutura.

c) Teor de oxigênio

- Quanto menos oxigênio mais deslocada a curva TTTc para a direita (óxidos evitam crescimento do grão). Oxigênio provoca a redução de elementos como Mn e Si, deslocando a curva para TTTc para a esquerda.
- Por outro lado, óxidos com tamanho de 0,2 a 2 μm (0,4 μm ideal) favorecem a nucleação de ferrita acicular.

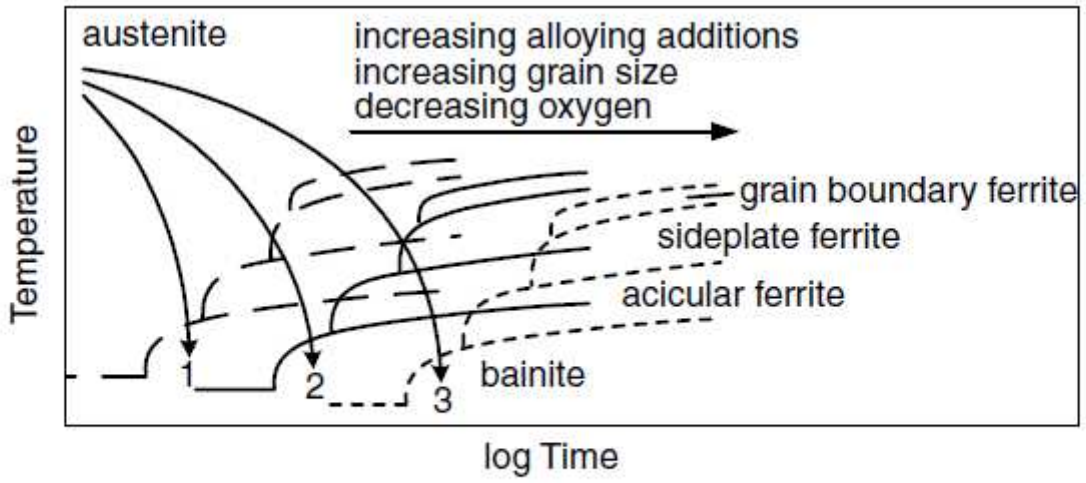

Figure 9.26 Effect of alloying elements, grain size, and oxygen on CCT diagrams for weld metal of low-carbon steel.

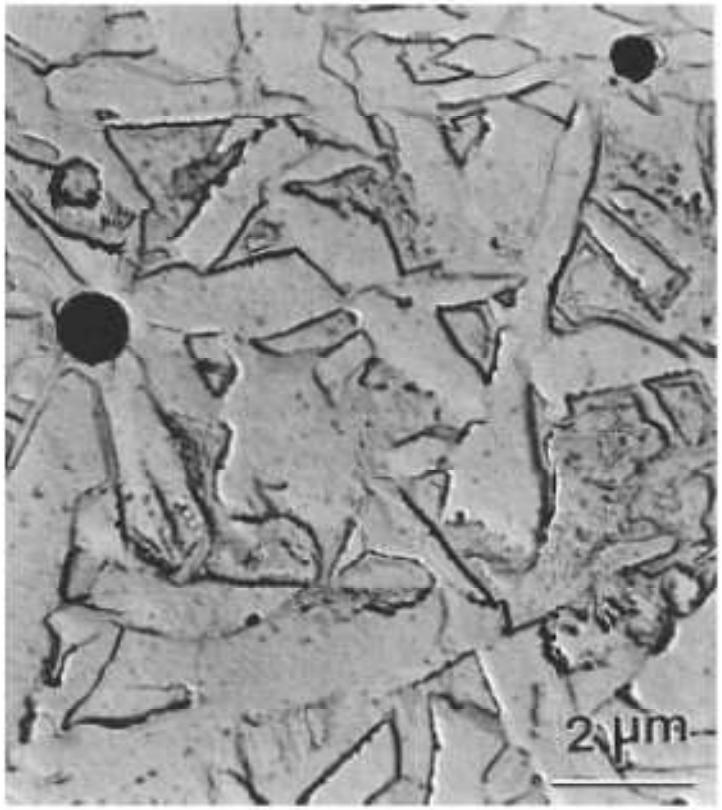

Figure 9.24 Acicular ferrite and inclusion particles in a low-carbon, low-alloy steel weld. Reprinted from Babu et al. (47).

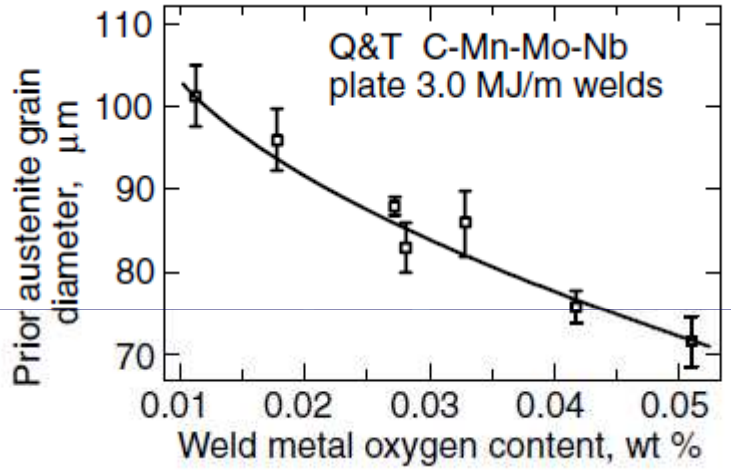

Figure 9.27 Prior austenite grain diameter as a function of weld metal oxygen content in submerged arc welds. Reprinted from Fleck et al. (49). Courtesy of American Welding Society.

Necessário portanto, otimizar % de oxigênio (ex. Solda MAG Ar-O_2 ou Ar-CO_2).

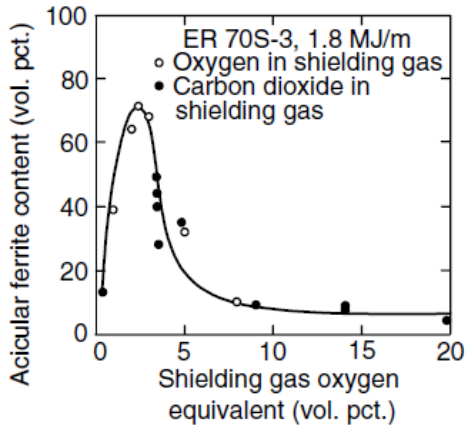

Figure 9.28 Acicular ferrite content as a function of shielding gas oxygen equivalent for gas–metal arc welds. Reprinted from Onsoien et al. (45). Courtesy of American Welding Society.

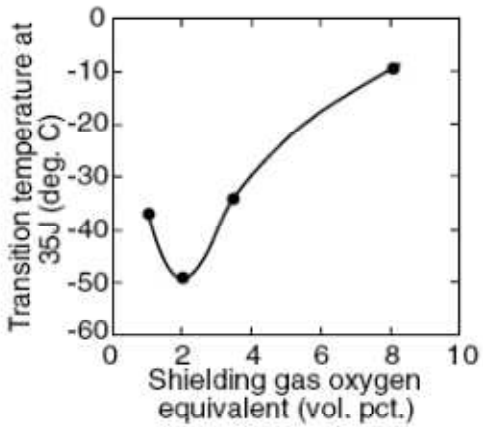

Figure 9.30 Weld metal Charpy V-notch toughness expressed as transition temperature as a function of shielding gas oxygen equivalent. Reprinted from Onsoien et al. (45). Courtesy of American Welding Society.

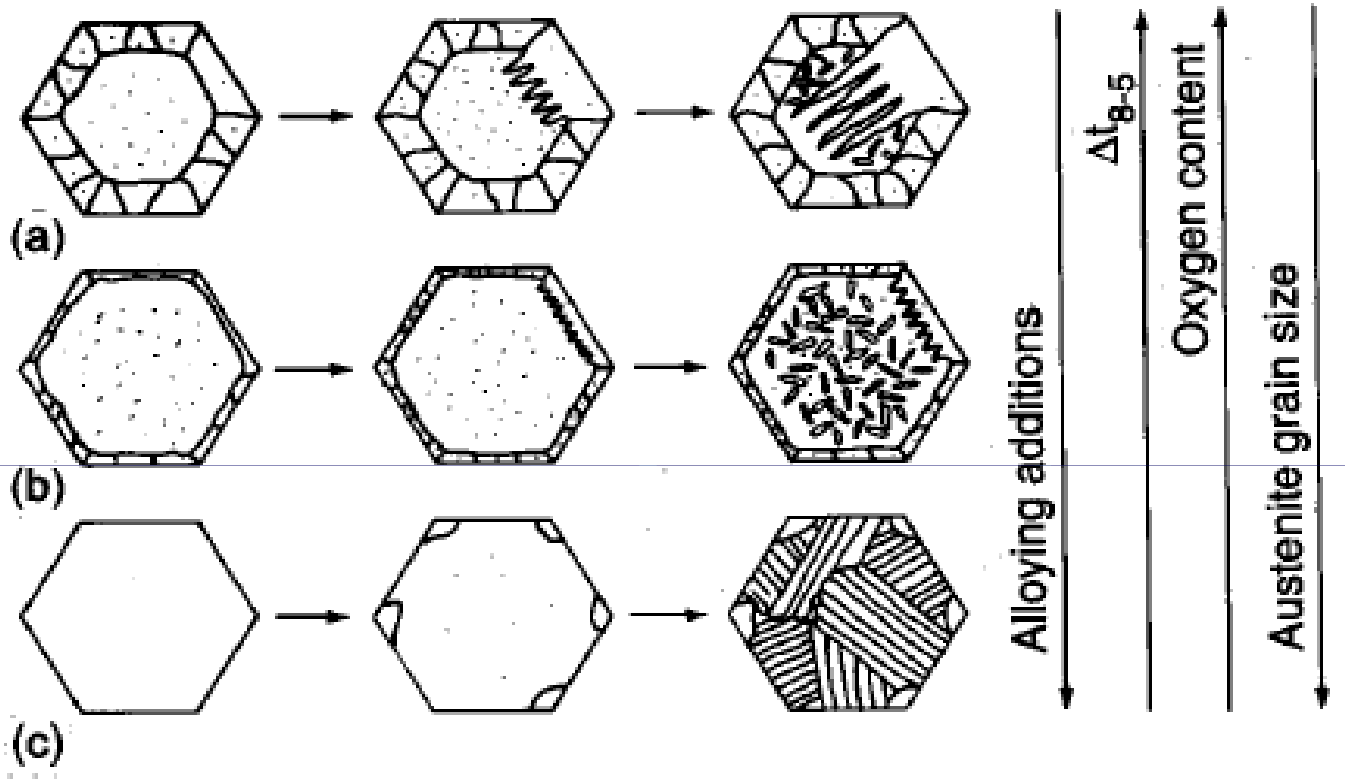

Figure 9.25 Schematic showing effect of alloy additions, cooling time from 800 to 500°C, weld oxygen content, and austenite grain size. Reprinted from Bhadeshia and Svensson (48).